Research Article Vol. 30, No. 5 / 28 Feb 2022 / Optics Express 8275

Optics EXPRESS

Phase-shifting algorithms with known and unknown phase shifts: comparison and hybrid

YUCHI CHEN AND QIAN KEMAO[*]

School of Computer Science and Engineering, Nanyang Technological University, Singapore 639798, Singapore

[*]*mkmqian@ntu.edu.sg*

Abstract: The phase-shifting interferometry has been intensively studied for more than half a century, and is still actively investigated and improved for more demanding precision measurement requirements. A proper phase-shifting algorithm (PSA) for phase extraction should consider various error sources including (i) the phase-shift errors, (ii) the intensity harmonics, (iii) the non-uniform phase-shift distributions and (iv) the random additive intensity noise. Consequently, a large pool of PSAs has been developed, including those with known phase shifts (abbreviated as kPSA) and those with unknown phase shifts (abbreviated as uPSA). While numerous evaluation works have been done for the kPSAs, there are very few for the uPSAs, making the overall picture of the PSAs unclear. Specifically, there is a lack of (i) fringe pattern parameters' restriction analysis for the uPSAs and (ii) performance comparison within the uPSAs and between the uPSAs and the kPSAs. Thus, for the first time, we comprehensively evaluated the pre-requisites and performance of four representative uPSAs, the advanced iterative algorithm, the general iterative algorithm (GIA), the algorithm based on the principal component analysis and the algorithm based on VU factorization, and then compare the uPSAs with twelve benchmarking kPSAs. From this comparison, the demand for proper selection of a kPSA, and the restriction and attractive performance of the uPSAs are clearly depicted. Due to the outstanding performance of the GIA, a hybrid kPSA-GIA is proposed to boost the performance of a kPSA and relieve the fringe density restriction of the GIA.

1. Introduction

Optical metrology plays an important role in precision engineering [1,2]. Among various techniques of optical metrology, phase-shifting interferometry [3,4] is known for its capability of full-field, non-contact, and high accuracy measurement, and has been intensively studied and widely used in both industry and academia for more than half a century [5–9]. In phase-shifting interferometry, the phase is directly related to the measured quantities such as shape [10], deformation [11], and refractive index [12]. A proper phase-shifting algorithm (PSA) that accurately extracts the phase from phase-shifted fringe patterns is essential, especially when one or multiple of the following common error sources present [6]: (i) the phase-shift errors caused by mis-calibration or imperfection of the phase-shifter [13], (ii) the intensity harmonics caused by nonlinearity of cameras and multi-beam reflections [14,15], (iii) the non-uniform phase-shift distributions caused by vibrations or air turbulence [16,17], and (iv) the random additive intensity noise caused by components of the optical system especially the detectors [18]. Although such error sources can be directly suppressed by high-quality components and/or optimized systems [8], choosing a PSA that is insensitive to these error sources is often a preferred solution. In fact, a big pool of PSAs with a wide variety has been developed [6–9].

The majority of PSAs adopt known phase shifts, extract the phase using trigonometric identities [5–9], and are abbreviated as kPSAs for convenience. They are simple and widely used. The digital Fourier transform algorithms (DFT) [4], the least squares algorithms (LSA) [19,20], the averaging algorithms (AVE) [21–23], the (N+1)-bucket algorithms (N+1) [24,25], the windowed

#452583 https://doi.org/10.1364/OE.452583
Journal © 2022 Received 29 Dec 2021; revised 10 Feb 2022; accepted 10 Feb 2022; published 25 Feb 2022

digital Fourier transform algorithms (WDFT) [26] and the generic error-compensating algorithms (GEC) [27] are such examples.

The other PSAs, which are abbreviated as uPSAs, adopt unknown phase shifts and thus are naturally immune to phase-shift errors. They can be further divided into three groups:

(i) The first group uses trigonometric identities for derivation, with the help of a regular phase shifts, *e.g.*, the Carré's algorithm (Carré) [3] and the Stoilov's algorithm [28], or the statistical properties of fringe patterns, *e.g.*, the Lissajous figure method [29,30], the phase statistics method [31] and the Euclidean matrix norm method [32]. Note that the forms of Carré and the Stoilov's algorithm are very similar to the kPSAs, and thus often evaluated together with kPSAs.

(ii) The second group adopts an optimization approach. The Okada's algorithm [33] uses an alternative linear least squares fitting framework to iteratively estimate the phase and the phase shifts. The advanced iterative algorithm (AIA) [34] improves the Okada's algorithm to make the phase extraction simple, robust and accurate. The Xu's algorithm [35], the Hoang's algorithms [36], the phase-tilt iteration algorithm [37] and the general iterative algorithm (GIA) [38] have been developed to further improve the AIA, by considering various error sources in the framework. With a similar approach, the model-based phase-shifting interferometry has been implemented in industrial applications [39].

(iii) The third group decomposes the fringe patterns into different components through linear algebra manipulations, such as the principal component analysis (PCA) [40], the Gram–Schmidt orthonormalization [41], the hyper-accurate ellipse fitting in subspace [42] and the VU factorization (VU) [43].

With a large number of PSAs available, examining them becomes critical for proper algorithm selection and performance boosting, and has been an important research topic. There are three main approaches on the evaluation of kPSAs. In the first approach, the performances of some selected PSAs with respect to various error sources are directly compared through simulation, including Creath's early study [5] and Buytaert *el al.*'s comprehensive comparison of 84 algorithms [7], among others [5–9]. In the second approach, Freischlad and Koliopoulos proposed the Fourier description method to evaluate the immunities of kPSAs to the phase-shift errors, the intensity harmonics and the random noise [44]. The Fourier description method was further generalized by Frequency Transfer Function method [45–47] which can be used to evaluate the immunity to the phase-shift error, the intensity harmonics and the random additive intensity noise. In the third approach, the kPSA's analysis and design are seamlessly combined through Larkin *et al.*'s [25] and de Groot's [48] frequency domain evaluation, Surrel's characteristic polynomials [26,49] and Hibino *et al.*'s equation solving [27,50–52], making the systematic algorithm design of error-compensating algorithms possible. Meanwhile, Servin *et al.* proposed a systemic approach to design kPSAs with irregular phase shifts by using the Frequency Transfer Function [53]. As for the uPSA, the simulation examination on the AIA's performance [54], the theoretical analysis on the PCA [55] and the modeling and optimization framework of the GIA [38] can be seen as examples of the above three evaluation approaches, respectively. However, such works are much fewer than those for the kPSA.

Therefore, while there is sufficient evaluation within kPSAs, there is an obvious lack of comprehensive evaluations and comparisons within uPSAs and between uPSAs and kPSAs. More specifically, the following aspects are not clear and need to be answered: (i) Are there any restrictions on the fringe patterns when we use the uPSAs? (ii) Which PSA has the best performance when the fringe patterns are with errors? and (iii) Is it possible to further improve the PSAs by combining the merits of the kPSAs and the uPSAs?

To answer these questions, we conduct a detailed examination of PSAs including the widely used kPSAs and the more recent uPSAs. For kPSAs, we select twelve algorithms with 3 to 15 steps [4,21,22,24,26,27,50,56,57] by considering their performances and representativeness, with their details given in Sec. 2.1. For the uPSAs, we select Carré [3] due to its simplicity, the AIA [34] and the PCA [40] due to their fundamental ideas, the GIA [38] and the VU [43] due to their robustness and outstanding accuracy. The following contributions are made:

(i) A detailed simulation evaluation to clarify the pre-requisites of the uPSAs on fringe pattern parameters is carried out;

(ii) Comprehensive comparisons within uPSAs and also between the uPSAs and the kPSAs are given, both for the first time, to provide a clear and big picture of their advantages and disadvantages;

(iii) A hybrid kPSA-GIA which use the kPSAs to initialize the GIA, and use the GIA to extract the phase is proposed.

The rest of the paper is arranged as follows. The selected PSAs in different categories are introduced in Sec. 2. The pre-requisites of the uPSAs are studied in Sec. 3, based on which, comprehensive comparisons within the uPSAs and between the uPSAs and the kPSAs are given in Sec. 4 and Sec. 5, respectively. The hybrid kPSA-GIA is proposed and validated in Sec. 6. An experiment is carried out in Sec. 7. The conclusions are drawn in Sec. 8. As many acronyms are used in this paper, they are listed in Table 1 for easy reference.

Table 1. List of acronyms.

Aberrations	Explanation	Aberrations	Explanation
AIA	Advanced iterative algorithm	N+1	(N+1)-bucket algorithm
AVE	Averaging algorithm	PCA	Phase-shifting algorithm based on principal component analysis
Carré	Carré's algorithm	PSA	Phase-shifting algorithm
DFT	Digital Fourier transform algorithm	PVE	Peak and valley of a phase error
GEC	Generic error-compensating algorithm	STDE	Standard deviation value of a phase error
GIA	General iterative algorithm	STD	Standard deviation
kPSA	Phase-shifting algorithm with known phase shifts	uPSA	Phase-shifting algorithm with unknown phase shifts
LSA	Least squares algorithm	VU	Phase-shifting algorithm based on VU factorization
ME	Mean value of a phase error	WDFT	Windowed digital Fourier transform algorithm

2. Selected PSAs

In this section, the PSAs selected for analysis and comparison are briefly introduced.

2.1. kPSAs

The fringe patterns used in PSAs are generally modeled as [6]

$$I(x,y;i) = A(x,y) + B(x,y)\cos[\varphi(x,y) + \delta(x,y;i)], \tag{1}$$

where $(x,y;i)$ represents the spatial-temporal coordinates with $x=0,1,\ldots,N_x-1$ and $y=0,1,\ldots,N_y-1$ corresponding to pixel location index and $i=0,1,\ldots,F-1$ corresponding to frame index; N_x is the total number of rows; N_y is the total number of columns; F is the total number of frames; I is the fringe intensity; A and B are the background intensity and the fringe amplitude, respectively; φ is the phase information; and δ is a phase shift which can be introduced actively or passively.

In the kPSAs, the pixel-independent phase shifts are actively introduced as

$$\delta(x, y; i) = \delta(i) = (i - \mathit{\Gamma})\omega, \tag{2}$$

where ω is the phase-shift increment, *i.e.* the phase shift difference between any two consecutive frames, and $\mathit{\Gamma}$ is the parameter which controls the phase origin, *i.e.* there is no shift of phase at the $\mathit{\Gamma}$-th frame. We call this special frame as the frame of the phase origin [9]. Most kPSAs use the first frame, *i.e.*, $\mathit{\Gamma}$ =0, or the middle frame, *i.e.*, $\mathit{\Gamma}$=(F-1)/2 as the frame of phase origin. Based on trigonometric identities, the phase is extracted by a weighted combination of the phase-shifted fringe patterns as [9]

$$\varphi(x, y) = \tan^{-1}\left[\frac{S(x, y)}{C(x, y)}\right] = \tan^{-1}\left[\frac{\sum_{i=0}^{F-1} s(i)I(x, y; i)}{\sum_{i=0}^{F-1} c(i)I(x, y; i)}\right], \tag{3}$$

where S and C are the numerator and denominator of the arctangent function, respectively; and $s(i)$ and $c(i)$ are the weights for the i-th frame. As can be seen, the kPSAs are pixel-wise and has the flexibility to work with different fringe densities, different background intensities and different fringe amplitudes. Thus, its only pre-requisite on fringe pattern parameter is that the phase shifts should be known. Since the kPSAs have been well developed [26,27,44–46,49–52] and intensively evaluated [5–9], only the following typical kPSAs are selected as representatives for a benchmarking purpose:

(i) The classic kPSAs with small step numbers ($F = 3{\sim}5$) which are convenient to use. We select the 3-step and the 4-step algorithms by Bruning *et al.* [4] and the 5-step algorithm by Schwider *et al.* [21]. These kPSAs are listed as the first three algorithms in Table 2.

(ii) The popular families of the kPSAs specified with a median step number of $F = 7$. The noticeable families included the DFT [4], the AVE [22], the N+1 [24], the WDFT [26] and the GEC [27]. Since they are specified at the same frame number, they can be fairly compared to showcase the interesting variety and to highlight the importance of the algorithm selection in phase-shifting interferometry. These kPSAs are listed as the next five algorithms in Table 2.

(iii) The kPSAs with good performances and large step numbers ($F = 9{\sim}15$). We select the 9-step algorithm by Hibino *et al.* [27] which has a good immunity to phase-shift non-uniformities, the 10-step algorithm by Surrel [26] and the 11-step algorithm by Hibino et al. [50,56] (with a minus sign as indicated by [26]) which has a good immunity to both up to the forth order intensity harmonics and the linear phase-shift errors, and the 15-step algorithm by De Groot et al. [57] which has a good immunity to even order intensity harmonics and random noise. These kPSAs are listed as the last four algorithms in Table 2.

The Surrel's characteristic polynomial plots of these kPSAs which are computed based on [26] are also shown in the last column of Table 2. These plots show the roots of the characteristic polynomials as illustrated by circles and can be used to quickly understand the kPSAs' error immunity. The two most useful conclusions of the characteristic polynomial plots are: (i) when there is no phase-shift error, a kPSA is insensitive to an intensity harmonic of k-th order ($k > 1$) if there are roots at both k and $2\pi/\omega$-k at the unit circle; and (ii) when there is a linear phase-shift error, a kPSA is insensitive to an intensity harmonic of k-th order ($k > 1$) if there are multiple roots at both k and $2\pi/\omega$-k, and more roots mean better immunity. In both cases, when $k = 1$, only $2\pi/\omega$-1 needs to be considered. For example, for the 5-step algorithm in Table 2, ω=π/2 and $2\pi/\omega$=4. This algorithm is insensitive to the second order harmonic ($k = 2$) when there is no

Table 2. Selected kPSAs for evaluation.

Name	F	ω (rad)	Γ	Parameter s and c	CP plot[a]
3-step [4]	**3**	**2π/3**	**1**	$\frac{\sqrt{3}\times[1,0,-1]}{1,2,1}$	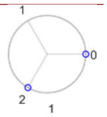
4-step [4]	**4**	**π/2**	**0**	$\frac{0,1,0,1}{1,0,1,0}$	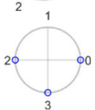
5-step [21]	**5**	**π/2**	**0**	$\frac{0,-2,0,2,0}{1,0,2,0,1}$	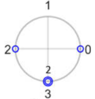
DFT [4]	**7**	**2π/7**	**0**	$\frac{\sin\left(i\times\frac{2\pi}{7}\right)(i=0-6)}{\cos\left(i\times\frac{2\pi}{7}\right)(i=0-6)}$	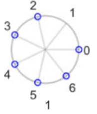
AVE [22]	**7**	**π/2**	**0**	$\frac{1,6,5,20,5,6,1}{1,4,15,0,15,4,1}$	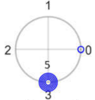
N+1 [24]	**7**	**π/3**	**0**	$\frac{1,3,3,0,3,3,1}{\sqrt{3}\times[1,1,-1,-2,-1,1,1]}$	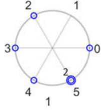
WDFT [26]	**7**	**π/2**	**3**	$\frac{1,0,3,0,3,0,1}{0,2,0,4,0,2,0}$	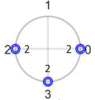
GEC [27]	**7**	**2π/5**	**3**	$\frac{0.263,0.325,0.951,0,0.951,0.325,0.263}{0.0854,0.724,0.309,1,0.309,0.724,0.0854}$	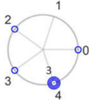
9-step [27]	**9**	**π/2**	**4**	$\frac{-1,2,14,18,0,-18,-14,-2,1}{-2,-8,-8,8,20,8,-8,-8,-2}$	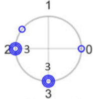
10-step [26]	**10**	**π/3**	**0**	$\frac{\sqrt{3}\times[-1,-3,-3,1,6,6,1,-3,-3,-1]}{1,1,7,11,6,6,11,7,1,1}$	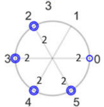
11-step [50,56]	**11**	**π/3**	**5**	$\frac{-\sqrt{3}\times[0,-1,-4,-7,-6,0,6,7,4,1,0]}{-2,-5,-6,-1,8,12,8,-1,-6,-5,-2}$	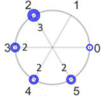
15-step [57]	**15**	**π/2**	**7**	$\frac{1,0,9,0,21,0,29,0,29,0,21,0,9,0,1}{0,4,0,15,0,26,0,30,0,26,0,15,0,4,0}$	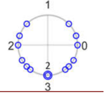

[a] A number k outside the unit circle indicates that the roots located there has an argument of $k\omega$, while a number k inside the unit circle indicates the number of roots at the same location.

phase-shift error, because there is a root at $k = 2$ and $2\pi/\omega\text{-}k = 4\text{-}2 = 2$. It is also insensitive to a linear phase-shift error since there are two roots at $2\pi/\omega\text{-}1 = 4\text{-}1 = 3$. Besides, seven kPSAs in Table 2 are analyzed in [49], while the other five are either from other famous families (the DFT, the AVE and the GEC) or newly proposed (9-step and 15-step).

A special PSA worth mentioning is Carré [3]. The fringe model for this algorithm follows Eqs. (1) and (2) with $F = 4$, $\Gamma = 1.5$ and an unknown ω. By using triangular identities and assuming $\omega\in[0, \pi]$, it has been derived that [58]

$$\varphi(x,y) = \tan^{-1}\left\{\frac{\sqrt{\begin{array}{c}\{3\,[I(x,y;2) - I(x,y;3)] - [I(x,y;1) - I(x,y;4)]\}\\ \times [I(x,y;2) - I(x,y;3)] + [I(x,y;1) - I(x,y;4)]\end{array}}}{[I(x,y;2)+I(x,y;3)]-[I(x,y;1)+I(x,y;4)]}\right\}. \tag{4}$$

In this algorithm, the best phase increment is ω=1.92 rads (110°) [59]. Nevertheless, we set $\omega=\pi/2$ rad, which is most often used. Noting that, since the phase shifts are unknown, Carré is a uPSA. However, in the rest of this paper, Carré is treated as one of the kPSAs for convenience due to the following reasons: (i) Comparing Eq. (4) and Eq. (3) shows that the form of Carré is similar to the other kPSAs; (ii) Furthermore, although the phase-shift increment ω is unknown, it remains constant; and (iii) Finally, Carré is a 4-step algorithm, unlike other uPSAs which can be applied to any sufficient numbers of frames.

2.2. uPSAs

Although less used, the uPSAs emerge as good competitors of the kPSAs. In this work, we select the AIA, the GIA, the PCA and the VU as representatives for evaluation.

2.2.1. AIA [34]

The AIA uses the fringe pattern model shown in Eq. (1) with unknown pixel-independent phase shifts, *i.e.* $\delta(x,y;i)=\delta(i)$. In the AIA, we set the frame of the phase origin at the first frame, *i.e.* $\delta(0) = 0$. The AIA iteratively estimates the phase φ and the phase shifts δ, until a convergence condition is satisfied.

The first step of the AIA estimates the phase in a pixel-wise manner. By treating the phase shifts as known and assuming that both the background intensity and the fringe amplitude are constant across frames, the fringe pattern model can be rewritten as

$$I(x,y;i) = a(x,y) + b(x,y)\cos[\delta(i)] + c(x,y)\sin[\delta(i)], \tag{5}$$

where $a(x,y)=A(x,y)$; $b(x,y)=B(x,y)\cos[\varphi(x,y)]$ and $c(x,y) = -B(x,y)\sin[\varphi(x,y)]$. For each pixel, the unknowns $a(x,y)$, $b(x,y)$ and $c(x,y)$ could be obtained from multiple linear equations with different index i and can be easily solved by linear least squares fitting with an inversion of a 3×3 matrix. Afterwards, the phase $\varphi(x,y)$ can be calculated from $b(x,y)$ and $c(x,y)$.

The second step estimates the phase shifts in a frame-wise manner. By treating the phase as known and assuming that both the background intensity and the fringe amplitude are constant across pixels in each frame, the fringe pattern model can be rewritten as

$$I(x,y;i) = a'(i) + b'(i)\cos[\varphi(x,y)] + c'(i)\sin[\varphi(x,y)], \tag{6}$$

where $a'(i)=A(i)$; $b'(i)=B(i)\cos[\delta(i)]$ and $c'(i) = -B(i)\sin[\delta(i)]$. Again, the unknowns $a'(i)$, $b'(i)$ and $c'(i)$ can be estimated by linear least squares fitting. Then, the phase shift of the i-th frame $\delta(i)$ can be calculated from the $b'(i)$ and $c'(i)$.

The AIA initializes the phase shifts based on prior knowledge or as random values casted within $[0, 2\pi]$. The stopping criteria is either the absolute phase shift changes of all the frames are sufficiently small, *i.e.*,

$$|[\delta^m(i) - \delta^m(0)] - [\delta^{m-1}(i) - \delta^{m-1}(0)]| < \varepsilon, \tag{7}$$

or the maximum iteration number is reached

$$m > M, \tag{8}$$

where $|\cdot|$ takes the absolute value, ε is a pre-set error tolerance, the superscript m indicates the number of iterations, and M is the pre-set maximum iteration number.

The AIA requires at least half a fringe within a frame for convergence [54]. As the AIA assumes the uniformity of the background intensity and the fringe amplitude, an error will occur when this assumption is violated, but it is not seen to be significant [60].

2.2.2. GIA [38]

It is interesting to see that the AIA estimates the unknown phase shifts together with the phase, making the algorithm insensitive to the phase-shift error. However, the AIA is still sensitive to the other types of error sources. Hence, following a similar framework, the recently proposed GIA more ambitiously incorporates all the concerned error sources into the fringe model and estimates them together with the phase.

Based on their different natures, the unknowns in the GIA are classified into three groups: (i) the background intensity and the fringe amplitude, (ii) the phase and (iii) the phase-shifts related parameters. Subsequently, these three groups of unknowns are optimized alternatively by the Levenberg-Marquart method, which has demonstrated excellent convergence and accuracy. In addition, the background intensity and the fringe amplitude can be separately estimated within a small window with a window size of $(2w+1)\times(2w+1)$, so that they are no longer required to be constant in the entire image, yet robust to noise. A typical size is $w = 5\sim10$ and we use $w = 8$ in this paper. The GIA can be conveniently initialized by the AIA or other PSAs. In later sections, we use the AIA for initialization thus need more than half a fringe within the frame. Meanwhile, we also notice that the GIA has a phase error when the background intensity and the fringe amplitude are discontinues which will be shown in Sec. 3.

2.2.3. PCA [40]

The PCA follows the AIA's fringe model, except that there is no specification on the frame of the phase origin. The PCA first removes the background intensity by subtracting the temporal average intensity, *i.e.*, $A(x, y) \approx \sum_{i=0}^{F-1} I(x, y; i)/F$. Furthermore, if the following approximation is well satisfied,

$$\sum_{y=0}^{N_y-1} \sum_{x=0}^{N_x-1} \{B(x, y) \cos[\varphi(x, y)]\}\{B(x, y) \sin[\varphi(x, y)]\} \approx 0, \tag{9}$$

then, viewing from the entire image, $B\sin(\varphi)$ and $B\cos(\varphi)$ are orthogonal to each other and can be considered as two most significant principal components of the background-intensity-removed fringe patterns [40]. Thus, the task of the phase extraction becomes the estimation of these two principal components, which can be easily achieved by PCA.

To do so, the background-intensity-removed fringe pattern intensities of the i-th frame are taken column-wisely to form a row vector with a length of $N_x\times N_y$. Next, the F row vectors from the F fringe patterns are stacked to form an $F\times(N_x\times N_y)$ matrix $\mathbf{D}$ whose entries are $D_{ij} = I(x,y;i)\text{-}A(x,y)$ with j is correlated to the pixel location (x,y) through $j = N_y x + y$. Subsequently, the following covariance matrix $\mathbf{C} = \mathbf{D}\times\mathbf{D}^T$ with a size of $F\times F$ can be diagonalized through singular value decomposition where the superscript T represents matrix transpose. Next, based on the Hotelling transform [61], the principal components of $\mathbf{D}$ can be extracted. The two principal components with the largest eigenvalues are corresponding to the sine and cosine terms of phase and can be used to extract the phase.

The PCA has two restrictions as indicated in its evaluation [55]: (i) There should be more than one fringe in the image so that the orthogonality assumption in Eq. (9) is valid; and (ii) the phase shifts must be well distributed in the $[0\ 2\pi]$ interval range so that the temporal averaging well estimates the background intensity and the principle components can be well decomposed [55]. These two restrictions will be evaluated through simulations in Sec. 3. Besides, the PCA has a mean error problem since the frame of the phase origin cannot be specified.

2.2.4. VU [43]

The VU views fringe patterns in a similar way as the PCA, but the background intensity is not pre-removed. As such, the VU rewrites the fringe model with reshaped matrices as follows,

$$\mathbf{I} = \mathbf{V}\mathbf{U}^T = \begin{pmatrix} \mathbf{a} & \mathbf{c} & -\mathbf{s} \end{pmatrix} \begin{pmatrix} \mathbf{1}^T \\ \mathbf{u}^T \\ \mathbf{v}^T \end{pmatrix}, \tag{10}$$

where the matrix $\mathbf{V}$ has a dimension of $(N_x \times N_y) \times 3$; the three vectors $\mathbf{a}$, $\mathbf{c}$ and $\mathbf{s}$ have respective entries $a_j = \mathrm{A}(j)$, $c_j = B(j)\cos[\varphi(j)]$ and $s_j = B(j)\sin[\varphi(j)]$; j has the same definition as the one in the PCA; the matrix $\mathbf{U}$ has a dimension of $3 \times F$; the vector $\mathbf{1}$ is a vector filled with ones; the vectors $\mathbf{u}$ and $\mathbf{v}$ have respective entries of $u_i = \cos[\delta(\mathrm{i})]$ and $v_i = \sin[\delta(i)]$.

However, the VU does not follow the PCA's concept of principle components. Instead, it iteratively estimates two matrices $\mathbf{U}$ and $\mathbf{V}$ through pseudoinverse with the assumption that the other matrix is known, reminding us the framework of the AIA. The VU also needs the restrictions on fringe density which will be confirmed in Sec. 3.

3. Pre-requisites of the uPSAs

A significate merit of the uPSAs is that they can extract the phase from fringe patterns with random unknown phase shifts. However, this advantage is achieved at a cost. In fact, the uPSAs may result in significant phase errors due to specific fringe density, phase-shift distribution, background intensity or fringe amplitude. In contrast, the kPSAs' performances are not affected by these factors. Thus, it is necessary to understand these pre-requisites of the uPSAs on fringe pattern parameters (Sec. 3.2) before we carry out detailed comparisons. The main approach for our PSA evaluation is through simulation, which has been widely used and well-recognized. Details are given (Sec. 3.1) as the preparation for the rest of the paper.

3.1. Codes, fringe patterns and error measures

The implementation of the kPSAs is according to Eq. (3) and the weight parameters in Table 2, which is straightforward. Carré is implemented following Eq. (4) and Refs. [3,58]. The AIA and the GIA are coded following Refs. [34] and [38], respectively. The codes of the PCA and the VU have been made available by the respective original authors [40,43], which are directly adopted in this paper. The settings of the parameters in the AIA, the GIA and the VU follow Refs. [34,38,43].

Due to the complexity of our evaluation, we start with the following default specifications on the fringe patterns as a common ground: (i) The frame number is set as eight; (ii) The image size is set as $N_x = N_y = 1024$; (iii) The background intensity and the fringe amplitude are set as $A = 0.5$ and $B = 0.4$; (iv) The phase is simulated as

$$\varphi(x, y) = \omega_p \times \mathrm{peaks_s}(N_x, N_y) + \omega_x x + \omega_y y, \tag{11}$$

where $\omega_p = 10$, $\omega_x = 0$ and $\omega_y = 0.25$, $\mathrm{peaks_s}$ uses the MATLAB function "$\mathrm{peaks_s}$" and linearly scales the value into the range of [0, 2π]; (v) The phase shifts are randomly set as [38]

$$\delta_0 = \begin{bmatrix} 0 & 0.440 & 0.795 & 1.246 & 1.601 & 2.665 & 2.695 & 3.449 \end{bmatrix}. \tag{12}$$

The phase map and the first fringe pattern of the common ground are shown in Fig. 1.

With this default setting, we will vary one particular parameter within an interval while keeping the others at their default values, to evaluate how this parameter affects the uPSAs. Note that

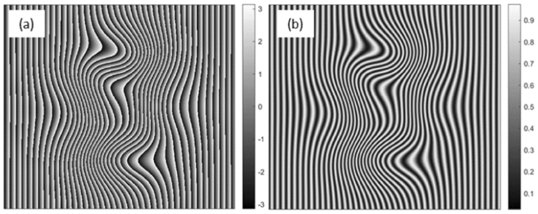

Fig. 1. The simulation parameters of the common ground. (a) The phase; (b) the first fringe pattern.

the phase shifts are purposely set the same as in [38]. However, we have extensively tried other random phase shifts, which give consistent conclusions.

The mean value of a phase error (ME) and the peak and valley of the phase error (PVE) are selected as two main error measures. Later on, when random noise presents, the standard deviation error (STDE) will also be used. Given the ground true value of φ_0 and the extracted phase φ, we denote the phase error as $\Delta\varphi{=}\varphi{-}\ \varphi_0$. The error measures are then defined as

$$\mathrm{ME} = \frac{\sum_{x,y}[\Delta\varphi(x,y)]}{N_x N_y}, \tag{13}$$

$$\mathrm{PVE} = \max_{x,y}[\Delta\varphi(x,y)] - \min_{x,y}[\Delta\varphi(x,y)], \tag{14}$$

$$\mathrm{STDE} = \sqrt{\frac{1}{N_x N_y - 1}\sum\nolimits_{x,y}[\Delta\varphi(x,y) - \mathrm{ME}]^2}. \tag{15}$$

3.2. Pre-requisites of the uPSAs on fringe pattern parameters

Unlike the kPSAs, we find that the uPSAs are affected by the fringe pattern parameters, *i.e.,* the spatial distributions of the phase φ, the fringe background A, and the fringe intensity B, as well as the angular distribution of the phase shifts δ. Thus, it is fundamental to understand their influences, or in other words, to clarify the pre-perquisites for uPSAs' safe usage. We seek these clarifications in this section where all the error sources do not present.

3.2.1. On the phase

The phase distribution affects the performance of the uPSAs. First, we focus on the global variation of the phase in the entire frame, which can also be represented by the total number of fringes (*i.e.*, 2π periods) per frame and is called as fringe density [54]. In our simulation following Sec. 3.1 with $\omega_p = 10$ and $\omega_x = 0$, we further express the parameter ω_y in the phase distribution in Eq. (11) as,

$$\omega_y = \frac{2\pi\tau_\varphi}{N_y - 1}, \tag{16}$$

where τ_φ indicates the fringe density, *i.e.*, there are τ_φ fringes in the entire frame. We vary ω_y from a fixed default value of 0.25 as set in Sec. 3.1 to an interval characterized by $\tau_\varphi \in (0, 3]$ to study its influence. In Fig. 2, three fringe patterns with τ_φ=0.5, τ_φ=1 and τ_φ=2 are shown.

The MEs and the PVEs of the phase extracted by the uPSAs are plotted against τ_φ in Fig. 3. The MEs of the AIA and the GIA are insignificant [38]. However, those of the PCA and the VU are large, and The large ME of the PCA has also been observed earlier in [42]. According to the PVEs, the fringe density should be higher than half a fringe in the frame ($\tau_\varphi \geq 0.5$) in order for the AIA, the GIA and the VU to perform accurately and stably. For the PCA, a fringe density of

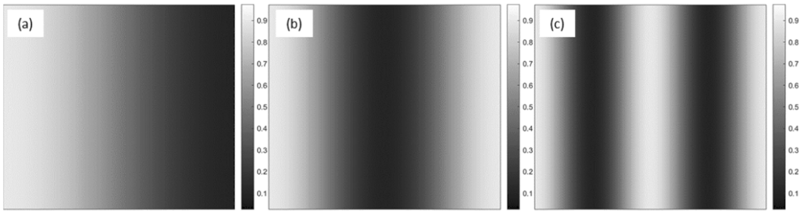

Fig. 2. The fringe patterns with different fringe density; (a) with τ_φ=0.5; (b) with τ_φ=1; (c) with τ_φ=2.

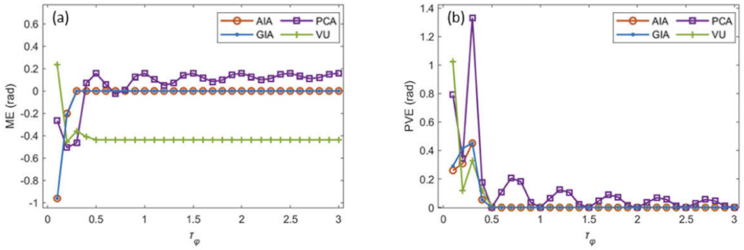

Fig. 3. The phase errors from fringe pattern with different fringe density. (a) The MEs; (b) the PVEs.

at least two fringes in the frame ($\tau_\varphi \geq 2$) is recommended so that d (9) can be satisfied to achieve a high accuracy, which is more stringent than the pre-requisite ($\tau_\varphi \geq 1$) given in [55].

We further study the distribution of the fringe, *i.e.*, the situation where the fringe is unevenly gathered in the frame. For this purpose, in the above simulation, we modify the phase as

$$\varphi(x, y) = \begin{cases} 2\pi\tau_\varphi y/\tau_\Phi(N_y - 1), & \text{if } y \leq \tau_\Phi(N_y - 1) \\ 0, & \text{if } y > \tau_\Phi(N_y - 1) \end{cases}, \tag{17}$$

where τ_Φ controls the area of the half a fringe and $\tau_\Phi \in [0.01, 1]$. We set τ_φ=0.5 for the AIA, GIA, and the VU and τ_φ=2 for the PCA. In Fig. 4, we show the phase and the first phase-shifted fringe pattern with τ_φ=0.5 τ_Φ=0.05, *i.e.* the half a fringe is concentrated within the left 5% area of the frame.

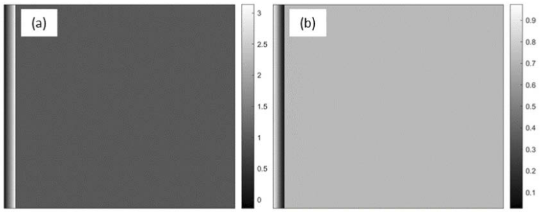

Fig. 4. The simulation parameters of a concentrated fringe pattern. (a) The phase; (b) the first fringe pattern.

The MEs and the PVEs of the phase extracted by the uPSAs are plotted against τ_Φ in Fig. 5. Even when the half a fringe is concentrated within 1% of the frame, the AIA, the GIA, and the VU can performance stably. However, the PVE of the PCA is large which demonstrates that the PCA performance badly when the fringe patterns are concentrated.

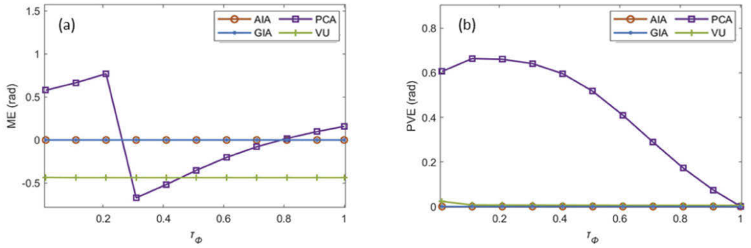

Fig. 5. The phase errors from a concentrated fringe pattern. (a) The MEs; (b) the PVEs.

There are a few remarks on the above results: (i) we also test the fringes with circular and other complex phases and obtain good consistency; (ii) the GIA's requirement for τ_φ<0.5 comes from that of the AIA because the AIA result is used to initialize the GIA. If a kPSA is used for initialization, then this pre-requisite is not necessary; (iii) as a byproduct, we notice that the phase in Eq. (17) is discontinuous between the two parts, none of the AIA, the GIA or the VU performs weirdly, especially around the discontinuity area. Meanwhile, we then carry out more simulations with different discontinuous phases fulfilling the fringe density requirement of τ_φ>0.5 for the AIA, GIA, and the VU and τ_φ>2 for the PCA, from which, it is confirmed that all these uPSAs are indeed insensitive to the phase discontinuities. For example, in the specific simulation according to Sec. 3.1, an additional phase of π/2 is added to the lower half of the fringe pattern so that there is a phase discontinuity of π/2 between the upper and lower halves. All the uPSAs produce their PVEs with an order of magnitude of 10^{-3} rad, which confirms that the uPSAs are not sensitive to simple phase discontinuities.

We now mention that, if a large ME from a particular algorithm is a concern in a certain measurement, then this algorithm should be used with caution. However, in many phase measurements, MEs are less important than PVEs [62]. We will thus discuss more on PVEs in the rest of the paper, while providing all the ME plots for reference.

3.2.2. On the phase-shift distribution

To see the influence of the phase-shift distribution, the fringe patterns are simulated according to Sec. 3.1, but the phase shifts are set as $\delta(i) = (i\pi/4)\times\tau_\delta$ ($i = 0\sim7$), *i.e.*, the phase shifts are evenly distributed within an interval of [0, 2π×τ_δ). For example, when τ_δ is 0.5, the phase shifts cover [0, π); when τ_δ is 1, they cover [0, 2π); when τ_δ is further increased to 2, they cover [0, 4π), or in other words, they cover [0, 2π) twice. The MEs and the PVEs of the uPSAs are plotted against τ_δ as shown in Fig. 6.

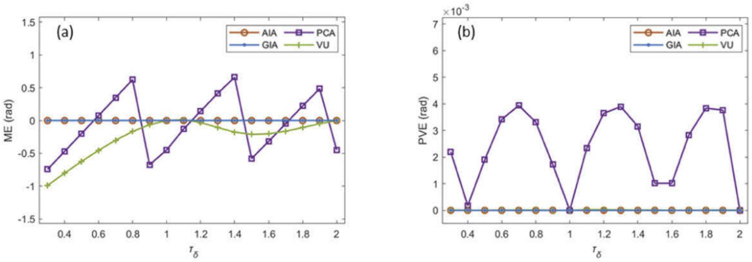

Fig. 6. The phase errors from fringe patterns with different phase shifts. (a) The MEs; (b) the PVEs.

All uPSAs' PVEs are in the order of 10^{-3} rad, showing that they are insensitive to the phase-shift distributions. Although the phase shifts used in Fig. 6 are all regular, random phase shifts are also tested in which we notice that all the uPSAs are insensitive to phase-shift distributions, as well expected. We highlight here that no error sources present in our pre-requisite study. In fact, when there are errors in the fringe patterns, phase-shift distributions evenly distributed with in [0, 2π) are preferred, which will be discussed in later sections.

3.2.3. On the background intensity and the fringe amplitude

To study the influence of the background intensity and the fringe amplitude, we first use the following model to make it spatially non-uniform,

$$A(x,y) = 0.5 - \frac{\tau_B y}{N_y - 1}, \tag{18}$$

where τ_B controls the non-uniformity level. Subsequently, the fringe amplitude is set as $B(x,y) = 0.8 \times A(x,y)$. The background intensity and the first fringe pattern with $\tau_B = 0.4$ are shown in Fig. 7.

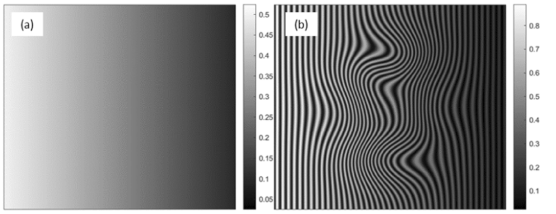

Fig. 7. The simulated parameters with highly non-uniform background intensity and fringe amplitude. (a) The background intensity; (b) the first fringe pattern.

The MEs and the PVEs of the uPSAs are plotted against τ_B as shown in Fig. 8. The GIA is least sensitive to the background intensity and the fringe amplitude non-uniformity, followed by the AIA. Although the PCA and the VU have no assumption on the background intensity and the fringe amplitude in theory, their performances are influenced by them.

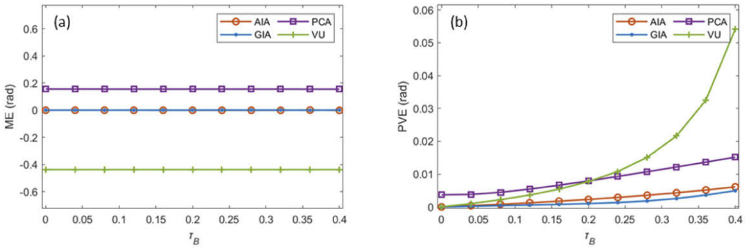

Fig. 8. The phase errors from fringe pattern with different non-uniform background intensity and fringe amplitude. (a) The MEs; (b) the PVEs.

Second, background intensity and fringe amplitude with a horizontal discontinuity are simulated as

$$A(x,y) = \begin{cases} 0.5 \text{ if } x \le N_x/2, \\ 0.25 \text{ if } x > N_x/2, \end{cases} \tag{19}$$

and $B(x,y) = 0.8 \times A(x,y)$. The background intensity with discontinuity and the first fringe pattern are shown in Fig. 9.

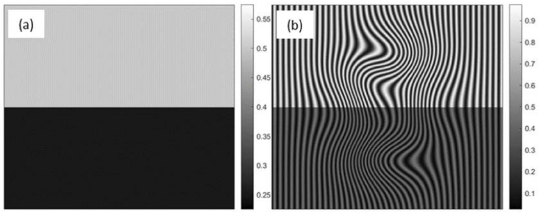

Fig. 9. The simulated parameters with discontinues background intensity and fringe amplitude. (a) The background intensity; (b) the first fringe pattern.

The phase error maps of the uPSAs are shown in Fig. 10. The middle columns of the phase error results from the uPSAs are shown in Fig. 11. Except the GIA, all the uPSAs' PVEs are in the magnitude of 10^{-3} rad. The GIA has an error at the discontinuity line because it assumes the uniformity of the background intensity and the fringe amplitude within a small window ($w = 8$ in this case). The other uPSAs are not sensitive to discontinuity in the background intensity and the fringe amplitude. As a remedy for the GIA, one may simply use a 1×1 window, *i.e.,* $w = 0$, to make the algorithm insensitive to the discontinuities. However, this practice will sacrifice the GIA's immunity to random noise and is only suggested when the random noise is not significant in the fringe patterns. Another possible remedy is that, for simple and few discontinuities like in Fig. 9, one may segment the fringe pattern into a few regions based on the fringe background and/or amplitude estimated by the AIA. Then the GIA is used for phase extraction region by region.

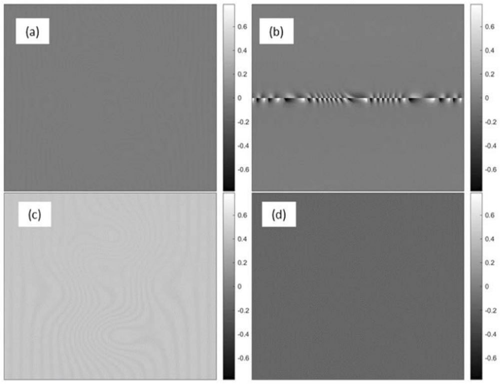

Fig. 10. The phase error maps from fringe pattern with discontinues background intensity and fringe amplitude: (a) the AIA; (b) the GIA; (c) the PCA; (d) the VU.

3.2.4. Summary

We summarize the pre-requisites of the uPSAs on fringe pattern parameters in Table 3. There are two main conditions that affect the uPSAs' performances. The first is when the fringe density is low, and the second (affect the GIA only) is when the background intensity and fringe amplitude are discontinues. Meanwhile, many fringe patterns, such as those from optical element and wafer testing, do not fall into these two conditions. Bearing these in mind, we now proceed to detailed comparisons when various error sources present.

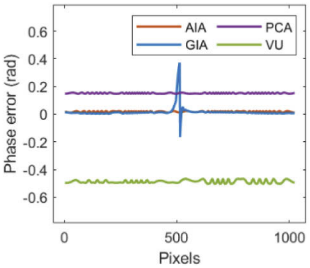

Fig. 11. The middle column of phase error map of the uPSAs from fringe patterns with discontinues background intensity and fringe amplitude.

Table 3. The pre-requisites of the uPSAs on fringe pattern parameters.

Fringe parameters		AIA	GIA	PCA	VU
Phase	Fringe density	≥0.5	≥0.5 (initialized by AIA); Free (initialized by the kPSAs)	≥2	≥0.5
Background intensity and fringe amplitudes	Non-uniformities			Slightly sensitive	Slightly sensitive
	Discontinuities		Sensitive (in general); Insensitive (if a 1×1 window is used or fringe patterns are segmented)		

4. Within the uPSAs: the performances with unknown phase shifts

Based on the pre-requisite study above, in later simulations, we set up two fringe pattern simulation restrictions: (i) The background intensity and the fringe amplitude are continuous; and (ii) Fringe density is higher than two fringes per image. To evaluate the performance of the uPSAs with various error sources, one error source at a time will be added into the fringe patterns simulated based on the default specifications discussed in Sec. 3.1, for detailed study. More tests with different fringe patterns will be carried out afterwards to support the study.

4.1. Phase-shift errors

In the kPSAs, the phase shifts are added actively, but the introduced values may deviate from their respective nominal values, *i.e.*, phase-shift errors occur. Typically, the mismatch between the true and nominal values includes both a pixel-independent part and a pixel-dependent part. The former is normally referred as a phase-shift error whose impact to the uPSAs is discussed in this subsection, while the latter is normally referred as phase-shift non-uniformity whose impact will be discussed in Sec. 4.3.

The phase-shift errors are introduced as additive noise with a mean of zero and a standard deviation of σ_δ=0~2π/4. The MEs and the PVEs of the uPSAs are plotted against σ_δ in Fig. 12. When σ_δ>π/4, the phase-shift errors are considered serious, but the obtained PVEs of all uPSAs are smaller than 5×10^{-3} rad, which is natural as the uPSAs are designed for unknown random phase-shifts, thus are perfectly insensitive to phase-shift errors.

4.2. Intensity harmonics

The intensity harmonics are added by using a gamma model, *i.e.*, I^γ is used to represent the fringe patterns with nonlinearity, where different values of γ=1~3 are simulated and γ=1 means there is no such error [63]. The fringe patterns with γ=1, γ=1.5 and γ=3 are shown in Fig. 13.

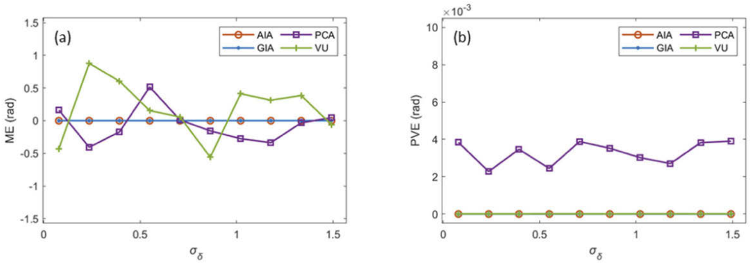

Fig. 12. The phase errors from fringe pattern with different amplitude of the phase-shift errors. (a) The MEs; (b) the PVEs.

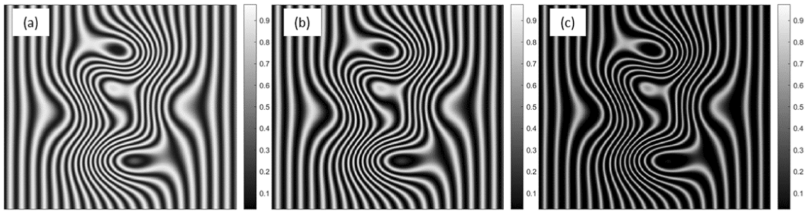

Fig. 13. The fringe pattern with intensity harmonics: (a) with γ=1; (b) with γ=1.5; (c) with γ=3.

The MEs and the PVEs of the uPSAs are plotted against γ in Fig. 14. With the increment of γ, the PVEs of all uPSAs increase. The GIA shows the best immunity to the intensity hormonic followed by the AIA, the PCA and the VU.

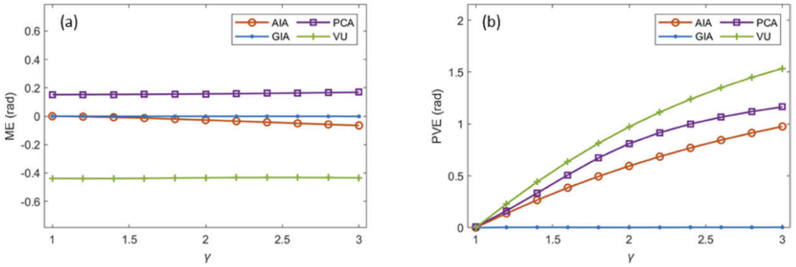

Fig. 14. The phase errors from fringe pattern with random phase shifts and different amplitude of the intensity harmonics. (a) The MEs; (b) the PVEs.

Besides, with the presence of the intensity harmonics, the phase-shift distribution plays a more significant role. The MEs and the PVEs of simulations according to Sec. 3.2.2 with intensity harmonics of γ=1.5 are shown in Fig. 15. It is clear now that the phase shifts should evenly distributed within [0, 2π). The GIA is seen as an exception. In general, making the phase shifts cover at least a full 2π interval is recommended for common practice.

Finally, we note that, our intension is to study the random phase-shift distributions, but the simulated phase shifts are regular. Nevertheless, when the random phase shifts approach a regular distribution which is nearly evenly distributed within [0, 2π), the error measures are better than the completely random phase shifts case. In other words, when the random phase shifts are introduced, we should make them cover a full 2π interval with nearly even distribution, if possible, for better error immunity to intensity harmonics. Similar preference on the phase shifts is also noticed in simulations with the presence of random noise.

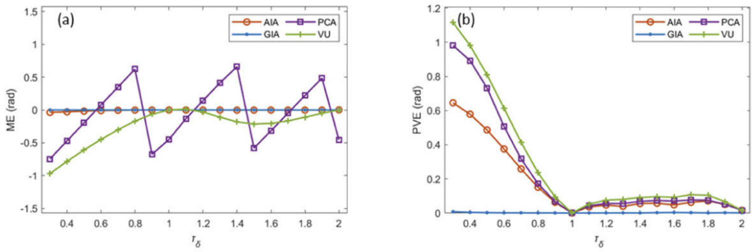

Fig. 15. The phase errors from fringe pattern with regular phase shifts and different amplitude of the intensity harmonics. (a) The MEs; (b) the PVEs.

4.3. Phase-shift non-uniformities

Different phase-shift non-uniformities are simulated as

$$\delta(x, y; i) = \sum\nolimits_{u=0}^{Q} \sum\nolimits_{v=0}^{u} \frac{\alpha_{uv}(i) x^v y^{u-v}}{(N_x - 1)^v (N_y - 1)^{u-v}}, \tag{20}$$

with different Q and different α_{uv}. For demonstration, first, a group of base $\bar{\alpha}_{uv}$ with $u = 0,\ldots,Q$, $v = 0,\ldots,u$ and $Q = 4$ is simulated as random values with a mean of zero and a standard deviation of σ_α=1. Next, the different amplitudes of phase-shift non-uniformities are simulated based on Eq. (20), with

$$\alpha_{uv} = \tau_\alpha \bar{\alpha}_{uv}, \tag{21}$$

and α_{00}=δ_0 in Eq. (12). The phase shifts of the second and last frame of fringe when τ_α=0.15 are shown in Fig. 16.

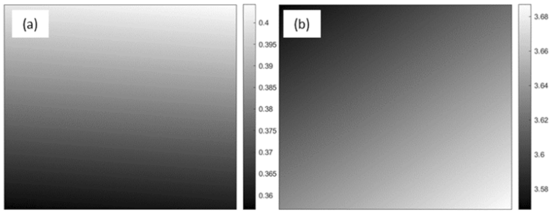

Fig. 16. The phase shifts with nonuniformities. (a) The second frame; (b) the last frame.

The MEs and the PVEs of the uPSAs are plotted against τ_α in Fig. 17. The GIA is the only algorithm considers the phase-shift non-uniformities and therefore has the best performance. The other three uPSAs have similar PVEs which increase significantly with respect to τ_α.

4.4. Random noise

Random noise is unavoidable in a real measurement. It is simulated as additive white Gaussian noise which has a mean of zero and a standard deviation of σ_I. Different amplitudes of random noise are simulated as $\sigma_I = 0 \sim 0.2$ (corresponding to 0%~50% of fringe amplitude). The first fringe patterns with different level of random noise of $\sigma_I = 0$, $\sigma_I = 0.04$ and $\sigma_I = 0.20$ are shown in Fig. 18.

The MEs and the STDEs of the uPSAs are plotted against σ_I in Fig. 19. The STDEs are linearly related to the noise level for all the uPSAs. When the noise is minor, the performances of all the uPSAs are similar. However, when the noise becomes heavier, the GIA shows a better immunity, while the other three uPSAs have a similar STDE performance due to their similar

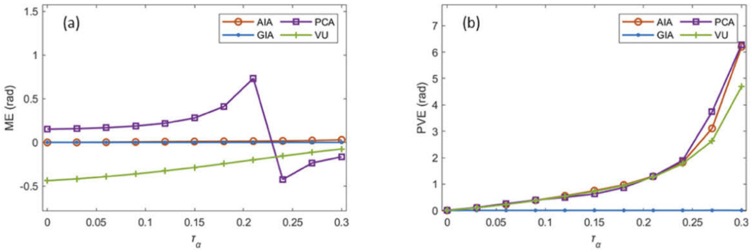

Fig. 17. The phase errors from fringe pattern with different level of phase-shift non-uniformities. (a) The MEs; (b) the STDEs.

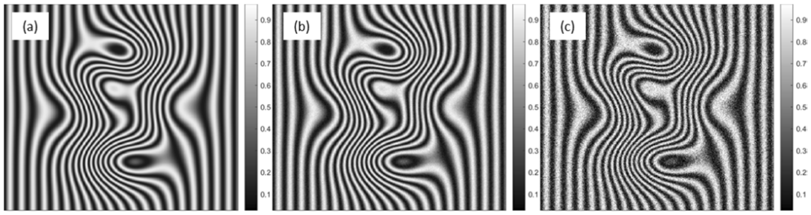

Fig. 18. The fringe pattern with random noise: (a) with $\sigma_I = 0$; (b) with $\sigma_I = 0.04$; (c) with $\sigma_I = 0.20$.

least squares nature. The better performance of the GIA is due to the averaging effect in the window-based background intensity and fringe amplitude estimation.

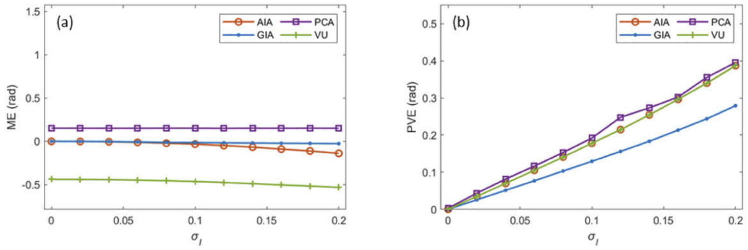

Fig. 19. The phase errors from fringe pattern with different level of random noise. (a) The MEs; (b) the STDEs.

We also study the influence of the frame number with the presence of random noise. Simulations are carried out according to Sec. 3.1 with a random noise $\sigma_I = 0.04$, regular phase shifts of $\delta(i) = 2i\pi/F$, and different frame numbers F. The MEs and the STDEs of the phases extracted by the uPSAs are plotted against F as shown in Fig. 20. Clearly, more fringe patterns should be acquired if higher accuracy is desired. In addition, the preference on phase shifts who are evenly distributed within [0, 2π) is also noticed in the simulation with random noise.

4.5. More tests and the summary

In the evaluation above, we focus on the default specifications discussed in Sec. 3.1. We further test 250 base sets of fringe patterns with: (i) different phase distributions simulated based on Eq. (11) with $\omega_p = 0{\sim}20$, $\omega_x = 0{\sim}0.5$ and $\omega_y = 0{\sim}0.5$; (ii) different background intensity simulated based on Eq. (18) with $\tau_B = 0{\sim}0.4$ and fringe amplitude as $B(x,y) = 0.8{\times}A(x,y)$; (iii) Different frame number as $F = 3{\sim}20$; (iv) Different phase shifts simulated as random value casted

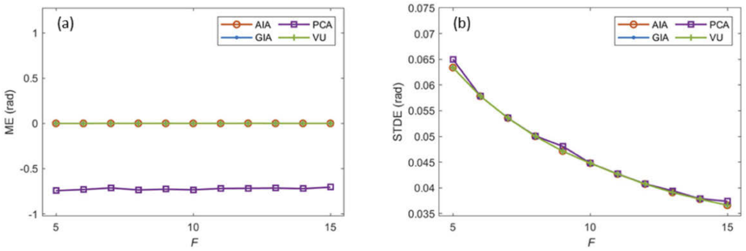

Fig. 20. The phase errors from fringe pattern with different frame number and random noise. (a) The MEs; (b) the STDEs.

with in [0, 2π) or specially set as $\delta(i) = 2i\pi/F\times\tau_{\delta}$. The error sources are added into them one by one, as described in Secs. 4.1~4.4, and then the performances of the uPSAs are compared. The previous results shown in Secs. 4. 1~4. 4 are typical. The main conclusions are as follows:

(i) In general, regular phase shifts evenly distributed within [0, 2π) are preferred and recommended for better immunity to the intensity harmonics and the random noise.

(ii) All the uPSAs prefer lower amplitude intensity harmonics, phase-shift non-uniformities and random noise. Thus, minimizing these error sources during testing, if possible, is recommended.

(iii) All the uPSAs have better noise suppression with more fringe patterns, and thus, capturing more fringe patterns is recommend, if time consumption is not an issue.

(iv) The GIA shows an outstanding performance due to the fact that it explicitly incorporates all the mentioned error sources into the fringe model and then explicitly estimates through optimization. Nevertheless, it suffers from the discontinuity problem in general.

5. Between the uPSAs and the kPSAs: the performance with known phase shifts

The uPSAs were developed for random unknown phase shifts. However, given the actively controlled known phase-shift values, the uPSAs can still work by treating them as unknown values. This provides a common scenario that uPSAs can be compared with the benchmarking kPSAs. We continue to use simulations to compare the uPSAs and the kPSAs. The default specifications on the fringe patterns are similar to those described in Sec. 3.1 except that the frame numbers and phase shifts are simulated based on the restrictions of the kPSAs and Carré. For the kPSAs, the frame numbers and phase shifts follow Table 2; for Carré, the frame number is set as $F = 4$ and the phase-shift increment ω is set as π/2 rad. We emphasize that the phase shifts in this section are regular, in contrast to the random ones in Sec. 4.

5.1. Phase-shift errors

Following the requirement of the kPSAs, the phase shifts are simulated according to Eq. (2). Furthermore, the phase shifts with a mis-calibration/detuning error are included as [7,35]

$$\delta(i) = (i - \mathit{\Gamma})\omega + \zeta(i), \tag{22}$$

with

$$\zeta(i) = \varepsilon_1(i - \mathit{\Gamma})\omega + \varepsilon_2(i - \mathit{\Gamma})^2\omega^2, \tag{23}$$

where $\xi(i)$ is the phase-shift error of the i-th frame, ε_1 and ε_2 are linear and quadratic error coefficients, respectively. Two cases are simulated: (i) linear miscalibration with $\varepsilon_1 = 0.05$ and

$\varepsilon_2 = 0$ and (ii) quadratic miscalibration with $\varepsilon_1 = 0$ and $\varepsilon_2 = 0.025$. The MEs and the PVEs of all the selected kPSAs and the uPSAs are shown in Fig. 21, where one kPSA only works for one particular frame number, while each uPSA is applicable to all frame numbers. The following are observed:

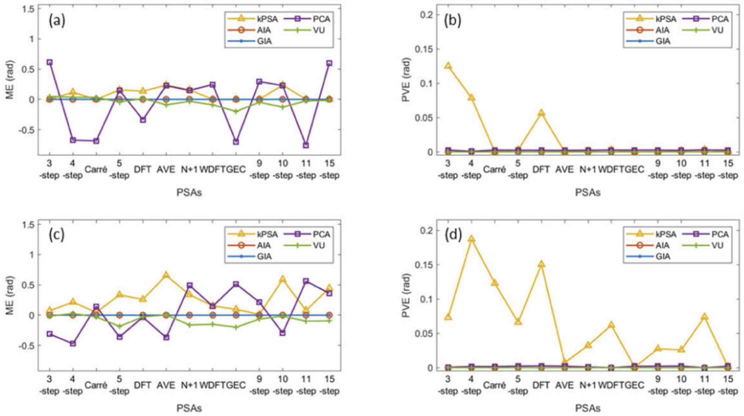

Fig. 21. The phase errors from fringe pattern with phase-shift errors. (a) The MEs with linear phase-shift errors; (b) the PVEs with linear phase-shift errors; (c) the MEs with quadratic phase-shift errors; (d) the PVEs with quadratic phase-shift errors.

- For the kPSAs, different algorithms give different PVEs, and thus choosing a proper algorithm is important, as has been well-understood and practiced. Most kPSAs, except the 3-step, the 4-step and the DFT, have good immunities to the linear phase-shift error, but only the AVE, the GEC and the 15-step have good immunities to the quadratic phase-shift error. These observations are consistent with the evaluation through the equation solving method [27,50–52]. If one wishes to select a proper kPSA systematically, Surrel's characteristic polynomials [26,49], Hibino et al.'s equation solving [27,50–52] and Servin et al.'s Frequency Transfer Function method [45–47] are recommended.
- For the uPSAs, the AIA, the GIA, the PCA and the VU have small PVEs, as expected. All the uPSAs perform much better than the kPSAs.

5.2. Intensity harmonics

The intensity harmonics are added by using a gamma model similar to the simulations in Sec. 4.2. We use γ=1.5 as an example. Due to this nonlinearity, the second and third order of harmonics appear, with their respective amplitudes about 10% and less than 1% of that of the first harmonic. There are also higher order harmonics with even smaller amplitudes. The MEs and the PVEs of the kPSAs and the uPSAs are shown in Fig. 22, from which the following are observed:

- For the kPSA, based on the theoretical evaluation through the characteristic polynomials [26], the DFT, the N+1, the GEC, the 10-step and the 11-step have good immunities to both the second and third order intensity harmonics, thus have the smallest PVEs; the 4-step, the 5-step, the 9-step, the WDFT and the 15-step have immunities only to the second order intensity harmonic, and thus, have the second tier PVEs; the 3-step and the AVE have no immunity to the second and third order intensity harmonics at all, and thus, have the worst PVEs. Carré is close to the worst tier.
- For the uPSAs, the AIA, the PCA and the VU have a much worse performance than the GIA and the well-performing kPSAs.

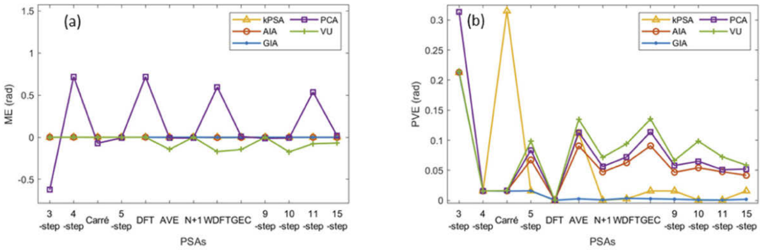

Fig. 22. The phase errors from fringe pattern with gamma. (a) The MEs; (b) the PVEs.

5.3. *Phase-shift non-uniformities*

To add the phase-shift non-uniformities, the phase shifts are simulated as [27]

$$\delta(x, y; i) = (i - \Gamma)\omega + \varepsilon_1(x, y)(i - \Gamma)\omega + \varepsilon_2(x, y)(i - \Gamma)^2\omega^2. \tag{24}$$

This phase shift model has its similarity to the one used in the Sec. 5.1 except that ε_1 and ε_2 are pixel-dependent now. The ε_1 and ε_2 are simulated as

$$\varepsilon_1(x, y) = \alpha_{\varepsilon 11}\left[\frac{x}{(N_x - 1)}\right]^2 + \alpha_{\varepsilon 12}\left[\frac{x}{(N_x - 1)}\right]\left[\frac{y}{(N_y - 1)}\right] + \alpha_{\varepsilon 13}\left[\frac{y}{(N_y - 1)}\right]^2, \tag{25}$$

$$\varepsilon_2(x, y) = \alpha_{\varepsilon 21}\left[\frac{x}{(N_x - 1)}\right]^2 + \alpha_{\varepsilon 22}\left[\frac{x}{(N_x - 1)}\right]\left[\frac{y}{(N_y - 1)}\right] + \alpha_{\varepsilon 23}\left[\frac{y}{(N_y - 1)}\right]^2. \tag{26}$$

where $\alpha_{\varepsilon 11}$, $\alpha_{\varepsilon 12}$, $\alpha_{\varepsilon 13}$, $\alpha_{\varepsilon 21}$, $\alpha_{\varepsilon 22}$ and $\alpha_{\varepsilon 23}$ are set as random values with a mean of zero and a standard deviation of 0.01. The MEs and the PVEs of the kPSAs and the uPSAs are shown in Fig. 23, from which the following are observed:

- For the kPSAs, the 9-step is with best immunity to phase-shift non-uniformities which is consistent with the evaluation in [27].
- For the uPSAs, the GIA performs the best due to its explicit consideration of the phase-shift non-uniformity in the algorithm design.

5.4. *Random noise*

Random noise is added as additive white Gaussian noise with a mean of zero and a standard deviation of σ_I similar to the simulation in the Sec. 4.4. We set $\sigma_I = 0.04$ (10% of fringe amplitude). The MEs and the STDEs of the kPSAs and the uPSAs are shown in Fig. 24, from which the following are observed:

- For the kPSAs, the STDEs are slightly larger comparing to those of the uPSAs. The STDE has tendency to reduce with the increasing frame number. The DFT has the best immunity to random noise among those with the same frame number, which is consistent with theoretical evaluation based on the SNR of the kPSAs [47,51].
- For the uPSAs, all the algorithms have very similar performances, due to their common least squares nature. However, as has been shown in Fig. 19 in Sec. 4.4, when noise is high, the GIA shows slightly better noise suppression.

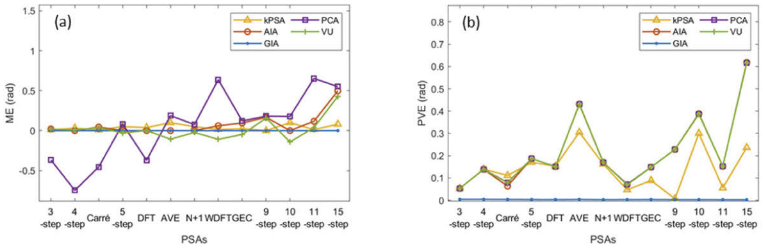

Fig. 23. The phase errors from fringe pattern with phase-shift non-uniformities. (a) The MEs; (b) the PVEs.

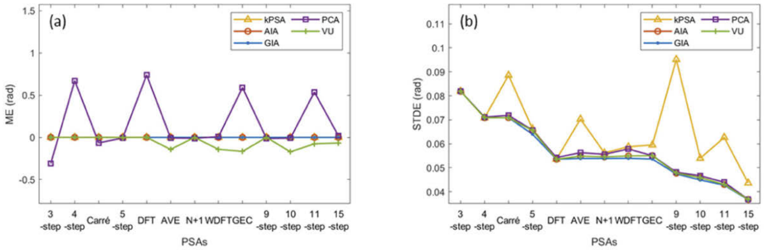

Fig. 24. The phase errors from fringe pattern with random noise. (a) The MEs; (b) the STDEs.

5.5. More tests and the summary

More tests with different phases, background intensities and fringe amplitudes, as described in Sec. 4.5, are carried out. The previous results shown in Secs. 5.1~5.4 are typical. Based on the evaluation, we summarize a few conclusions:

(i) The kPSAs, in general, do not show good immunities to the tested error sources. However, one can always find a suitable algorithm to tackle the presenting error source(s). For example, the DFT has the best error immunity to the random noise when frame number is fixed. Meanwhile, it is always possible to increase the frame number for better immunity to the random noise. Similarly, the AVE and the GEC show good immunities to the phase-shift errors up to quadratic order; The DFT, the N+1, the GEC, the 10-step and the 11-step have good immunities to the second and third order intensity harmonics; The 9-step is insensitive to phase-shift non-uniformities. These results hint the importance of proper algorithm selection, which may require deep understanding about the kPSAs.

(ii) The GIA consistently shows good immunities to all four tested error sources, as it is the only PSA incorporating these error sources. Besides, other uPSAs also show good immunities to the phase-shift error and the random noise.

(iii) The uPSAs have pre-requisites as shown in Sec. 3.2.4, which poses undesired uncertainty in a measurement or requires extra controls to satisfy these pre-requisites during the measurement. However, this paper sends a clear message that the uPSAs are very strong competitors and alternatives of the kPSAs. In particular, (a) when the pre-requires are satisfied, the uPSAs can very likely perform better than the kPSAs; and (b) in the adversary situation and environment where controlling phase-shifts is difficult, a high phase extraction accuracy can still be expected by a uPSA.

6. Hybrid kPSA-GIA

Based on the above extensive evaluations, especially the outstanding performance of the GIA, we further propose a hybrid kPSA-GIA, which uses a kPSA to extract the phase to initialize the GIA and uses the GIA to extract the phase again. Similar hybrid work can also be found in [39]. This hybrid kPSA-GIA can be interpreted from two viewpoints. From the first point of view, even when a kPSA is not properly selected and does not well compensate a certain error source, the subsequent GIA can serve as a refinement to improve the phase accuracy. From the other point of view, since in most phase-shifting interferometers, the phase shifts can be well controlled and known, a kPSA can be used to initialize the GIA. The pre-requisite of the GIA on the fringe density, one of the two pre-requisites of the GIA, is removed, which further improves the applicability of the GIA. In summary, the hybrid kPSA-GIA alleviates the difficulty of kPSA selection, improves the phase extraction accuracy of a kPSA, and removes the fringe density pre-requisite in the GIA. One may choose any suitable kPSAs for initialization to form hybrid algorithms such as AVE-GIA and WDFT-GIA.

To validate the advantages, we test all the simulation cases in Secs. 5.1~5.4 again by the hybrid kPSA-GIA. The phase error measures of the hybrid kPSA-GIA are very close to those by the AIA initialized GIA and are smaller than those by the original kPSAs. Besides, we also tested low density fringe patterns with the phase distribution simulated according to Eq. (11), Eq. (16), and with τ_φ<0.5. For all simulation conditions, the hybrid kPSA-GIA performs stably even with τ_φ=0. These results further confirm the effectiveness of the hybrid kPSA-GIA. Meanwhile, it is also worth mentioning that when the fringe density is very low, the error immunities to the intensity harmonics and the random noise of the hybrid kPSA-GIA are not as good as the results of the $\tau_\varphi \geq$0.5 cases because there are not enough intensity variation within the window for GIA's accurate estimation of the background intensity and the fringe amplitude. However, in such a case, it is reasonable to use a larger window size in the GIA for a better accuracy performance.

To demonstrate the effectiveness of the hybrid kPSA-GIA and its insensitivity to the fringe density, two sets of phase-shifted fringe patterns are specially tested. The first set is generated according to Sec. 5.2 with phase distribution according to Eq. (11), $\omega_p = 10$, $\omega_x = 0$ and $\omega_y = 0.25$ and serves as a case with normal fringe density (about 40 fringes per frame). The second set has a phase distribution according to Eq. (11), Eq. (16) and τ_φ=0.3, and serves as a case with low fringe density (0.3 fringes per frame). The first fringe patterns simulated under these conditions are shown in Fig. 25.

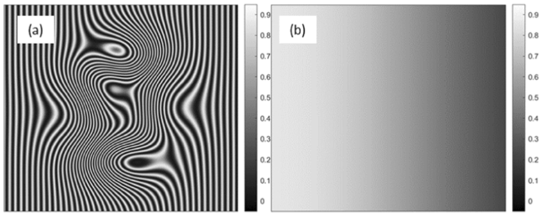

Fig. 25. The simulated fringe patterns: (a) with normal fringe density; (b) with low fringe density.

The PVEs of the kPSAs, the GIA and the hybrid kPSA-GIA of these two cases are shown in Fig. 26(a) and Fig. 26(b), respectively. In both figures, the PVEs of the kPSA (in yellow) have been successfully suppressed by the hybrid kPSA-GIA (in black). Furthermore, The GIA's PVEs in Fig. 26(b) are much worse than that in Fig. 26(a) because of the low fringe density, but it is successfully boosted by the PSAs' initialization.

Meanwhile, the GIA has an interesting capability and advantage that it can reconstruct the a noiseless fringe pattern following the complete fringe model given in [38], because the GIA

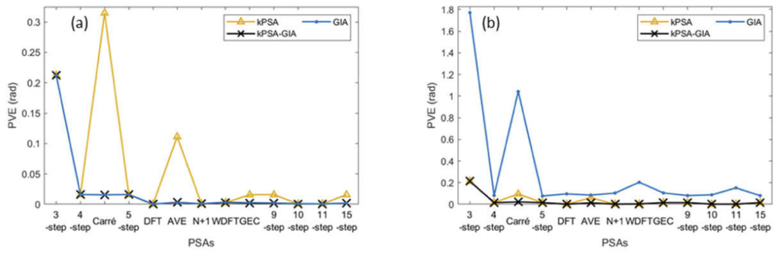

Fig. 26. The phase errors from fringe pattern with intensity harmonics. (a) The PVEs with normal fringe density; (b) the PVEs with low fringe density.

estimates all the parameters in this model. The difference between the reconstructed fringe pattern and the original fringe pattern can be used as an indicator of the GIA's performance on convergence and accuracy. The hybrid kPSA-GIA inherits this advantage. As an example, we simulate fringe patterns according to Sec. 5.2 with $F = 7$, $\omega = \pi/2$, $\Gamma = 0$, $\omega_p = 10$, $\omega_x = 0$ and $\omega_y = 0.25$, and use WDFT-GIA for phase extraction and fringe reconstruction. The first frame of the simulated phase-shifted fringe patterns, the first frame of the reconstructed fringe patterns and the difference between them are shown in Fig. 27. Clearly, the different between the simulated pattern and the reconstructed pattern has an order of magnitude of 10^{-4}, which indicates the good performance of the kPSA-GIA.

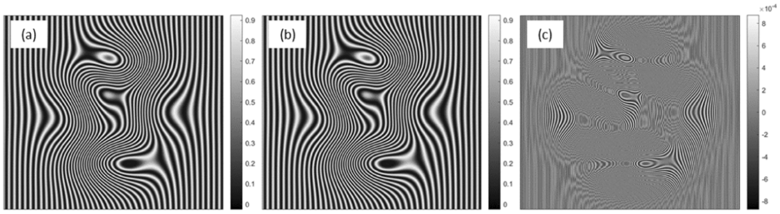

Fig. 27. The first fringe patterns. (a) The simulated; (b) the reconstructed; (c) the difference.

To ease the process of the kPSA selection, we recommend to use the LSA as the initializing kPSA for the hybrid kPSA-GIA, as the LSA can be used for any frame number and any phase shifts as long as they are known, which leads to an LSA-GIA. We tested the LSA-GIA again with the simulation cases in Fig. 26 and obtain similar error measures as those from the kPSA-GIA in that figure.

7. Experiments evaluation and the speed

An optical testing experiment is also carried out to verify the performance of the kPSAs, the uPSAs and the proposed kPSA-GIA. A Fizeau interferometer whose sketch is shown Fig. 28 is used for the test. A wedged optical window is used as the reference and a piece of silicon wafer is used as the test object. The phase shifts were introduced by tuning the wavelength of the interferometer's laser [64]. In the experiments, the frame size is $N_x = N_y = 1024$.

The AVE and the WDFT are selected to compare with the uPSAs and the kPSA-GIA due to their unique performance. Thus, we capture a set of seven fringe patterns with phase shifts of $i\pi/2$ $(0 \leq i \leq 6)$. Meanwhile, in this experiment, the intensity harmonics and the phase-shift non-uniformities are purposely introduced by controlling the nonlinear response of the camera with $\gamma=1.5$ [65] and exciting the mounting of the interferometer's reference by a mechanical actuator [16], respectively. The first, the fourth and the seventh frames are shown in Fig. 29.

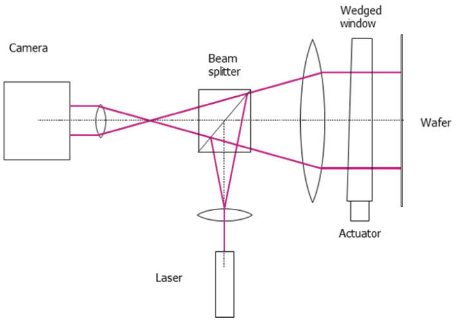

Fig. 28. The skitch of the Fizeau interferometer [38].

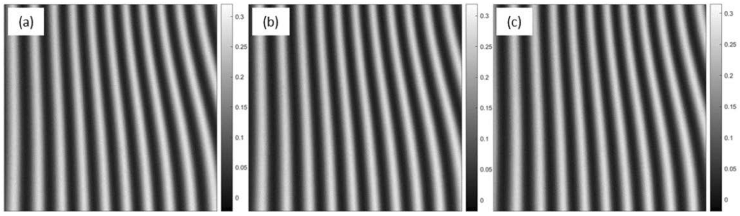

Fig. 29. A set of seven fringe patterns. (a) The first; (b) the fourth; (c) the seventh.

The AVE and the WDFT are used to form the hybrid algorithms of the AVE-GIA and the WDFT-GIA. These two hybrid algorithms together with the AVE, the WDFT, the AIA, the GIA, the PCA and the VU are used to process the fringe patterns. The middle row of the phases extracted by these PSAs are shown in blue in Fig. 30. The phase cross section is selected instead of the 2D phase maps for clearer demonstration of the differences of these PSAs. The phase results are increasing from left to right, so a common linear part is removed. Then, these phase results are filtered by a Gaussian-weighted moving average filter with a filter length of 100 pixels and a standard deviation of 20 pixels, as overlaid in red in Fig. 30. After we subtract the filtered phase from the raw phase in Fig. 30, we obtain the residuals whose standard deviation (STD) values are calculated and shown in the Table 4. The GIA and the respective hybrid kPSA-GIA, although initialized differently, give the same standard deviations, which are smaller than those from the kPSAs.

Table 4. Standard deviation value of the phase noise of first column (unit: rad) and computation time of each algorithm (unit: second).

	AVE	WDFT	AIA	GIA	PCA	VU	AVE-GIA	WDFT-GIA
STD	0.098	0.087	0.060	0.054	0.060	0.065	0.054	0.054
Time	0.083	0.079	14.84	713.12	0.52	1.13	1293.91	1392.74

Speed is another concern when using the PSAs in industrial application. The time consumptions of the AVE, the WDFT, the AIA, the GIA, the PCA, the VU, the AVE-GIA, the WDFT-GIA for extracting the phase from the experimental fringe patterns are shown in Table 4. The processing is carried out with MATLAB 2020a implementation on a workstation equipped with an Intel Xeon E5-2699 v3 processors (18 cores, 2.3Ghz main frequency) and 256 GB RAM. The kPSAs are much faster than the uPSAs. Among the uPSAs, the GIA is the slowest due to the iterations and the Levenberg-Marquart optimization method. As for the hybrid algorithms, the AVE-GIA and the WDFT-GIA are slower comparing to the GIA as the initializations by the AVE and the

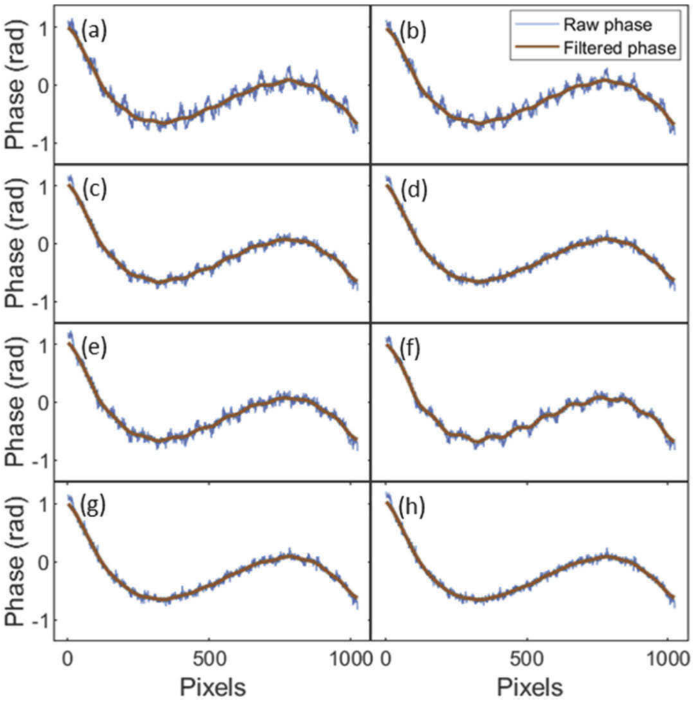

Fig. 30. The middle rows of the extracted phases by different algorithms. (a) The AVE; (b) the WDFT; (c) the AIA; (d) the GIA; (e) the PCA; (f) the VU; (g) the AVE-GIA; (h) the WDFT-GIA.

WDFT are worse than the initialization by the AIA. More specifically, there are 21 iterations for the AVE-GIA and WDFT-GIA and 10 iterations for the GIA. This slow speed of the hybrid algorism does not defeat the motivation of proposing the hybrid kPSA-GIA algorithms, as the results of the kPSAs are indeed improved by their respective hybrid ones. In this experiment, the fringe density is considered high, hence the accuracy difference between the GIA and the hybrid ones (the AVE-GIA and the WDFT-GIA) are not significate. If the AIA performance better than a kPSA in phase extraction, then the AIA initialized GIA is faster than the kPSA-GIA. However, when the fringe density is low, the kPSA-GIA provides significate advantage as shown in Sec. 6.

8. Conclusion

Phase shifting is an important technique in optical metrology. Many PSAs with known and unknown phase shifts have been proposed to extract the phase accurately from the phase-shifted fringe patterns. Although many performance evaluation and comparison works have been intensively carried out for the kPSAs, very few were done for the uPSAs. Thus, to further advance the phase-shifting technique, three geared investigations are carried out. We first study the pre-requisites of four uPSAs (the AIA, the GIA, the PCA and the VU) and find that certain fringe density is needed for all the uPSAs and the smoothness of the fringe background and intensity is required for the GIA. Next, we compare the performance of these uPSAs' with the presence of different error sources. All the uPSAs can extract phase successfully when the pre-requisites are fulfilled, among which, the GIA performs the best. Third, with this success, we move on to compare the uPSAs with twelve representative kPSAs. We find that, although it is always possible to find a suitable kPSA algorithm to tackle the presenting error source(s), the uPSAs, especially the GIA, can serve as a more convenient option and offer better results.

Finally, to utilize the excellent performance from the GIA, but to overcome the pre-requisite for fringe density, a hybrid kPSA-GIA is proposed and shown effective. From this study, we expect a significantly more intensive use of the uPSAs in both research and engineering applications.

Funding. Economic Development Board - Singapore (S17-1579-IPP-II); Ministry of Education - Singapore (MOE-T2EP20220-0008).

Disclosures. The authors declare no conflicts of interest.

Data availability. Data underlying the results presented in this paper are not publicly available at this time but may be obtained from the authors upon reasonable request.

References

1. W. Osten, "Optical metrology: the long and unstoppable way to become an outstanding measuring tool," in *Speckle 2018: VII International Conference on Speckle Metrology*, (International Society for Optics and Photonics, 2018), 1083402.
2. Y. Kim, K. Hibino, R. Hanayama, N. Sugita, and M. Mitsuishi, "Multiple-surface interferometry of highly reflective wafer by wavelength tuning," Opt. Express **22**(18), 21145–21156 (2014).
3. P. Carré, "Installation et utilisation du comparateur photoélectrique et interférentiel du Bureau International des Poids et Mesures," Metrologia **2**(1), 13–23 (1966).
4. J. H. Bruning, D. R. Herriott, J. Gallagher, D. Rosenfeld, A. White, and D. Brangaccio, "Digital wavefront measuring interferometer for testing optical surfaces and lenses," Appl. Opt. **13**(11), 2693–2703 (1974).
5. K. Creath, "Phase-measurement interferometry techniques," in *Prog. Opt.*, (Elsevier, 1988), pp. 349–393.
6. D. Malacara, *Optical shop testing* (John Wiley & Sons, 2007), Vol. 59, pp. 547–655.
7. J. A. N. Buytaert and J. J. J. Dirckx, "Study of the performance of 84 phase-shifting algorithms for interferometry," J. Opt. **40**(3), 114–131 (2011).
8. P. Rastogi and E. Hack, *Phase estimation in optical interferometry* (CRC, 2014), pp. 235–270.
9. D. Malacara, M. Servin, and Z. Malacara, *Interferogram analysis for optical testing* (CRC, 2018), pp. 359–398.
10. K. Okada, H. Sakuta, T. Ose, and J. Tsujiuchi, "Separate measurements of surface shapes and refractive index inhomogeneity of an optical element using tunable-source phase shifting interferometry," Appl. Opt. **29**(22), 3280–3285 (1990).
11. J. Degrieck, W. Van Paepegem, and P. Boone, "Application of digital phase-shift shadow moiré to micro deformation measurements of curved surfaces," Opt. Lasers. Eng. **36**(1), 29–40 (2001).
12. Y.-C. Chu, W.-Y. Chang, K.-H. Chen, J.-H. Chen, B.-C. Tsai, and K. Y. Hsu, "Full-field refractive index measurement with simultaneous phase-shift interferometry," Optik **125**(13), 3307–3310 (2014).
13. Y.-Y. Cheng and J. C. Wyant, "Phase shifter calibration in phase-shifting interferometry," Appl. Opt. **24**(18), 3049–3052 (1985).
14. R. Schödel, A. Nicolaus, and G. Bönsch, "Phase-stepping interferometry: methods for reducing errors caused by camera nonlinearities," Appl. Opt. **41**(1), 55–63 (2002).
15. P. Hariharan, "Digital phase-stepping interferometry: effects of multiply reflected beams," Appl. Opt. **26**(13), 2506–2507 (1987).
16. P. J. De Groot, "Vibration in phase-shifting interferometry," J. Opt. Soc. Am. A **12**(2), 354–365 (1995).
17. N. Bobroff, "Residual errors in laser interferometry from air turbulence and nonlinearity," Appl. Opt. **26**(13), 2676–2682 (1987).
18. M. Servin, J. Estrada, J. Quiroga, J. Mosiño, and M. Cywiak, "Noise in phase shifting interferometry," Opt. Express **17**(11), 8789–8794 (2009).
19. C. Morgan, "Least-squares estimation in phase-measurement interferometry," Opt. Lett. **7**(8), 368–370 (1982).
20. J. E. Greivenkamp, "Generalized data reduction for heterodyne interferometry," Opt. Eng. **23**(4), 234350 (1984).
21. J. Schwider, R. Burow, K.-E. Elssner, J. Grzanna, R. Spolaczyk, and K. Merkel, "Digital wave-front measuring interferometry: some systematic error sources," Appl. Opt. **22**(21), 3421–3432 (1983).
22. J. Schmit and K. Creath, "Extended averaging technique for derivation of error-compensating algorithms in phase-shifting interferometry," Appl. Opt. **34**(19), 3610–3619 (1995).
23. J. Schmit and K. Creath, "Window function influence on phase error in phase-shifting algorithms," Appl. Opt. **35**(28), 5642–5649 (1996).
24. Y. Surrel, "Phase stepping: a new self-calibrating algorithm," Appl. Opt. **32**(19), 3598–3600 (1993).
25. K. Larkin and B. Oreb, "Design and assessment of symmetrical phase-shifting algorithms," J. Opt. Soc. Am. A **9**(10), 1740–1748 (1992).
26. Y. Surrel, "Design of algorithms for phase measurements by the use of phase stepping," Appl. Opt. **35**(1), 51–60 (1996).
27. K. Hibino, B. F. Oreb, D. I. Farrant, and K. G. Larkin, "Phase-shifting algorithms for nonlinear and spatially nonuniform phase shifts," J. Opt. Soc. Am. A **14**(4), 918–930 (1997).
28. G. Stoilov and T. Dragostinov, "Phase-stepping interferometry: Five-frame algorithm with an arbitrary step," Opt. Lasers. Eng. **28**(1), 61–69 (1997).

29. C. T. Farrell and M. A. Player, "Phase step measurement and variable step algorithms in phase-shifting interferometry," Meas. Sci. Technol. **3**(10), 953–958 (1992).
30. C. Farrell and M. Player, "Phase-step insensitive algorithms for phase-shifting interferometry," Meas. Sci. Technol. **5**(6), 648–654 (1994).
31. L. Z. Cai, Q. Liu, and X. L. Yang, "Phase-shift extraction and wave-front reconstruction in phase-shifting interferometry with arbitrary phase steps," Opt. Lett. **28**(19), 1808–1810 (2003).
32. Y. Xu, Y. Wang, Y. Ji, H. Han, and W. Jin, "Three-frame generalized phase-shifting interferometry by a Euclidean matrix norm algorithm," Opt. Lasers. Eng. **84**, 89–95 (2016).
33. K. Okada, A. Sato, and J. Tsujiuchi, "Simultaneous calculation of phase distribution and scanning phase shift in phase shifting interferometry," Opt. Commun. **84**(3-4), 118–124 (1991).
34. Z. Wang and B. Han, "Advanced iterative algorithm for phase extraction of randomly phase-shifted interferograms," Opt. Lett. **29**(14), 1671–1673 (2004).
35. J. Xu, Q. Xu, and L. Chai, "An iterative algorithm for interferograms with random phase shifts and high-order harmonics," J. Opt. A: Pure Appl. Opt. **10**(9), 095004 (2008).
36. T. Hoang, Z. Wang, M. Vo, J. Ma, L. Luu, and B. Pan, "Phase extraction from optical interferograms in presence of intensity nonlinearity and arbitrary phase shifts," Appl. Phys. Lett. **99**(3), 031104 (2011).
37. M. Duan, Y. Zong, R. Zhu, and J. Li, "Phase-tilt iteration: Accurate and robust phase extraction from random tilt-shift interferograms," Opt. Lasers. Eng. **142**, 106595 (2021).
38. Y. Chen and Q. Kemao, "General iterative algorithm for phase-extraction from fringe patterns with random phase-shifts, intensity harmonics and non-uniform phase-shift distribution," Opt. Express **29**(19), 30905–30926 (2021).
39. L. L. Deck, "Model-based phase shifting interferometry," Appl. Opt. **53**(21), 4628–4636 (2014).
40. J. Vargas, J. A. Quiroga, and T. Belenguer, "Phase-shifting interferometry based on principal component analysis," Opt. Lett. **36**(8), 1326–1328 (2011).
41. W. Niu, L. Zhong, P. Sun, and X. Lu, "Phase shifts extraction algorithm based on Gram–Schmidt orthonormalization of two vectors," Opt. Quantum Electron. **47**(8), 2803–2810 (2015).
42. K. Yatabe, K. Ishikawa, and Y. Oikawa, "Simple, flexible, and accurate phase retrieval method for generalized phase-shifting interferometry," J. Opt. Soc. Am. A **34**(1), 87–96 (2017).
43. M. A. Escobar, J. C. Estrada, and J. Vargas, "Phase-shifting VU factorization for interferometry," Opt. Lasers. Eng. **124**, 105797 (2020).
44. K. Freischlad and C. L. Koliopoulos, "Fourier description of digital phase-measuring interferometry," J. Opt. Soc. Am. A **7**(4), 542–551 (1990).
45. M. Servin, J. C. Estrada, and J. A. Quiroga, "Spectral analysis of phase shifting algorithms," Opt. Express **17**(19), 16423–16428 (2009).
46. M. Servin, J. C. Estrada, and J. A. Quiroga, "The general theory of phase shifting algorithms," Opt. Express **17**(24), 21867–21881 (2009).
47. S. Ordones, M. Servin, M. Padilla, A. Muñoz, J. L. Flores, and I. Choque, "Spectral analysis for the generalized least squares phase-shifting algorithms with harmonic robustness," Opt. Lett. **44**(9), 2358–2361 (2019).
48. P. De Groot, "Derivation of algorithms for phase-shifting interferometry using the concept of a data-sampling window," Appl. Opt. **34**(22), 4723–4730 (1995).
49. Y. Surrel, "Additive noise effect in digital phase detection," Appl. Opt. **36**(1), 271–276 (1997).
50. K. Hibino, B. F. Oreb, D. I. Farrant, and K. G. Larkin, "Phase shifting for nonsinusoidal waveforms with phase-shift errors," J. Opt. Soc. Am. A **12**(4), 761–768 (1995).
51. K. Hibino, "Susceptibility of systematic error-compensating algorithms to random noise in phase-shifting interferometry," Appl. Opt. **36**(10), 2084–2093 (1997).
52. K. Hibino and M. Yamauchi, "Phase-Measuring Algorithms to Suppress Spatially Nonuniform Phase Modulation in a Two-Beam Interferometer," Opt. Rev. **7**(6), 543–549 (2000).
53. M. Servin, M. Padilla, G. Garnica, and G. Paez, "Design of nonlinearly spaced phase-shifting algorithms using their frequency transfer function," Appl. Opt. **58**(4), 1134–1138 (2019).
54. Y. Chen and Q. Kemao, "Advanced iterative algorithm for phase extraction: performance evaluation and enhancement," Opt. Express **27**(26), 37634–37651 (2019).
55. J. Vargas, J. A. Quiroga, and T. Belenguer, "Analysis of the principal component algorithm in phase-shifting interferometry," Opt. Lett. **36**(12), 2215–2217 (2011).
56. H. Canabal, J. A. Quiroga, and E. Bernabeu, "Improved phase-shifting method for automatic processing of moiré deflectograms," Appl. Opt. **37**(26), 6227–6233 (1998).
57. P. de Groot, "Measurement of transparent plates with wavelength-tuned phase-shifting interferometry," Appl. Opt. **39**(16), 2658–2663 (2000).
58. Q. Kemao, *Windowed fringe pattern analysis* (Society of Photo-Optical Instrumentation Engineers, 2013), pp. 1–20.
59. Q. Kemao, S. Fangjun, and W. Xiaoping, "Determination of the best phase step of the Carré algorithm in phase shifting interferometry," Meas. Sci. Technol. **11**(8), 1220–1223 (2000).
60. Z. Wang and B. Han, "Advanced iterative algorithm for randomly phase-shifted interferograms with intra-and inter-frame intensity variations," Opt. Lasers. Eng. **45**(2), 274–280 (2007).
61. L. N. Trefethen and D. Bau III, *Numerical linear algebra* (Siam, 1997), Vol. 50, pp. 25–31.

62. C. Ai and J. C. Wyant, “Effect of piezoelectric transducer nonlinearity on phase shift interferometry,” Appl. Opt. **26**(6), 1112–1116 (1987).
63. K. Liu, Y. Wang, D. L. Lau, Q. Hao, and L. G. Hassebrook, “Gamma model and its analysis for phase measuring profilometry,” J. Opt. Soc. Am. A **27**(3), 553–562 (2010).
64. L. L. Deck and J. A. Soobitsky, “Phase-shifting via wavelength tuning in very large aperture interferometers,” in *Optical manufacturing and testing III*, (International Society for Optics and Photonics, 1999), 432–442.
65. S. Zhang and S.-T. Yau, “Generic nonsinusoidal phase error correction for three-dimensional shape measurement using a digital video projector,” Appl. Opt. **46**(1), 36–43 (2007).